LAWRENCE
LIVERMORE
NATIONAL
LABORATORY

UCRL-PROC-233251

First principles calculation of point defects and mobility degradation in bulk AlSb for radiation detection application

V. Lordi, D. Aberg, P. Erhart, K. J. Wu

August 2, 2007

Hard X-Ray and Gamma-Ray Detector Physics VIII
San Diego, CA, United States
August 26, 2007 through August 30, 2007

Disclaimer

First principles calculation of point defects and mobility degradation in bulk AlSb for radiation detection application

Vincenzo Lordi*, Daniel Åberg, Paul Erhart, and Kuang Jen Wu

Lawrence Livermore National Laboratory, 7000 East Ave, Livermore, CA, USA

ABSTRACT

The development of high resolution, room temperature semiconductor radiation detectors requires the introduction of materials with increased carrier mobility-lifetime ($\mu\tau$) product, while having a band gap in the 1.4–2.2 eV range. AlSb is a promising material for this application. However, systematic improvements in the material quality are necessary to achieve an adequate $\mu\tau$ product. We are using a combination of simulation and experiment to develop a fundamental understanding of the factors which affect detector material quality. First principles calculations are used to study the microscopic mechanisms of mobility degradation from point defects and to calculate the intrinsic limit of mobility from phonon scattering. We use density functional theory (DFT) to calculate the formation energies of native and impurity point defects, to determine their equilibrium concentrations as a function of temperature and charge state. Perturbation theory via the Born approximation is coupled with Boltzmann transport theory to calculate the contribution toward mobility degradation of each type of point defect, using DFT-computed carrier scattering rates. A comparison is made to measured carrier concentrations and mobilities from AlSb crystals grown in our lab. We find our predictions in good quantitative agreement with experiment, allowing optimized annealing conditions to be deduced. A major result is the determination of oxygen impurity as a severe mobility killer, despite the ability of oxygen to compensation dope AlSb and reduce the net carrier concentration. In this case, increased resistivity is not a good indicator of improved material performance, due to the concomitant sharp reduction in $\mu\tau$.

Keywords: Mobility, carrier lifetime, aluminum antimonide, semiconductor, defect, impurity, formation energy, density functional theory

1. INTRODUCTION

High resolution, room temperature gamma radiation detectors are important for a variety of applications, including homeland security, nuclear nonproliferation and monitoring, medical imaging, and space imaging. The problem of developing such a detector is essentially a materials issue.[1,2] The use of semiconductors for the active material is particularly attractive, due to the wide spectrum of properties available and the ability to tune the properties over large ranges by, *e.g.*, doping, alloying, and thermal treatment. Several materials parameters are critical for the development of a gamma radiation detector that operates with high energy resolution at room temperature.

An appropriate band gap in the range of $\sim$1.4–2.2 eV is essential. The detector operates basically by counting the number of electron-hole pairs created in the semiconductor from an incident gamma ray. The number of carriers generated will be proportional to the ratio of the gamma ray energy to the band gap energy (divided by and ionization factor in the range of 2–3.5). It is generally desired to maximize the number of generated carriers to reduce the statistical counting noise (which varies as the square-root of the number); this requirement sets the practical upper bound of the desired band gap range. On the other hand, thermal excitation of valence electrons across the band gap will generate a number of carriers proportional to $\exp(-E_g/k_BT)$, where E_g is the band gap energy, k_B is Boltzmann's constant, and T is absolute temperature. The practical lower limit for the band gap is determined by the requirement to minimize the background signal from thermally generated carriers, enabling room temperature operation.

Furthermore, we generally require materials containing high-Z elements ($\gtrsim 50$) to efficiently stop high energy gamma rays in a practical volume of material. Roughly speaking, high performance gamma detection within a crystal volume on the order of 1–100 cm^3 is desired. Such a volume implies a required stopping length on the order of 1–10 cm. Moreover, the large crystal volume implies a requirement that carrier drift lengths in the material approach distances $\gg$1 cm, for highly efficient collection at the electrodes (*i.e.*, counting) of the generated carriers from each incident gamma ray. The resolution

*Send correspondence to V.L.: lordi2@llnl.gov; phone 1 925 423 2755

and energy range of the detector will depend on the ratio of the drift length to the device thickness.[3] Typically, a ratio of at least 100 is sought.

The requirement of very long carrier drift lengths in the semiconductor is the main issue in selecting and optimizing a material for radiation detection application, and is also the major basis of differentiation for the performance of different materials. The drift length, λ_d, in the semiconductor is related to the carrier mobility, μ, and the average carrier lifetime, τ, through $\lambda_d = \mu\tau E$, where E is the magnitude of the electric field in the crystal. The electric field is generally maximized in a device by applying a voltage close to the breakdown voltage of the material, which depends on its purity. Then, E will be determined by the applied voltage divided by the length between the contacts, and will not vary very much between materials of adequate purity for use in radiation detectors. On the other hand, μ and τ are material parameters that can vary greatly for a given material depending on the growth conditions, processing history, and levels of various defects. At relatively high temperatures ($i.e.$, room temperature), μ will be limited by electron-phonon scattering, but defects in the material can cause μ to be considerably lower than this upper bound. For high resolution detectors (***e.g.***, $\lesssim 1\%$ at 662 keV), a $\mu\tau$ product $\gtrsim 0.1$ cm^2/V is required. We will use $\mu\tau$ as a figure of merit which we seek to maximize for candidate radiation detector materials.

Growth of large, high purity, uniform single crystals is often difficult, and development efforts can be quite expensive. Currently, the best available semiconductor material for room temperature detection is CdZnTe (CZT), which can achieve energy resolution less than 1%. However, growth of CZT to-date produces extremely inhomogeneous crystals containing both microscopic and macroscopic defects. To achieve the highest performance from CZT requires careful harvesting of many small crystals with the desired materials properties (sometimes from multiple growths) and fabricating complex detector arrays to incorporate, in aggregate, the required crystal volume. The result is an impractically high materials cost due to the extraordinarily low yield of the best usable material, up to ~100,000 USD for a single detector.

We seek to use first principles calculations of materials properties in conjunction with experimental efforts of growth and post-growth heat treatment to accelerate the development cycle of new materials. Particularly, we seek to understand the theoretical limits of materials performance for radiation detection application in order to judge the suitability of a given material and also benchmark the quality of grown crystals. A detailed, mechanistic understanding of the nature and effects of various defects in the crystal enables a focused experimental effort in optimizing the material quality. The goal is to grow large, uniform single crystals, enabling potentially low cost, high resolution room temperature detectors.

AlSb, with a band gap of 1.61 eV at room temperature, is a promising candidate semiconductor to meet the requirements outlined above. Optimized growth of this material has been hindered by a host of defects that adversely affect the mobility. We are using a joint theoretical and experimental effort to understand the nature, concentration, and effects on mobility of the various defects, to systematically improve the quality of crystals and find optimized annealing conditions. In this paper, we focus on the native defects in AlSb, as well as O and C impurities. We use density functional theory (DFT) to calculate the equilibrium atomic structure of each defect, its formation energy, the equilibrium defect and carrier concentrations as functions of temperature, and the strength of mobility degradation related to each defect. We relate our predictions to measured properties of various large, high-purity AlSb single crystals grown in our lab. Particularly, we correlate minimum defect densities to equilibrium densities of native defects (particularly Al vacancies) and correlate measured values of carrier concentrations to the incorporation of oxygen impurities which compensate the naturally *p*-type material. We also predict that O impurities are particularly detrimental to carrier mobilities, consistent with experimental suggestions. Our calculations also lead to predictions of appropriate post-growth annealing temperatures. By annealing at 1200 K for 8 d, we have been successful in reducing carrier densities in our AlSb material to $\sim 3 \times 10^{13}$ cm^{-3} (partially compensated) and total defect densities to $\sim 3 \times 10^{16}$ cm^{-3}, with corresponding hole mobilities of a few hundred cm^2/V-s.

2. METHODOLOGY

2.1 Computational methods

We use density functional theory to study the stability of point defects in different charge states by calculating their equilibrium atomic structures and the corresponding total energies. We calculate defect formation energies to obtain equilibrium concentrations of each defect as a function of temperature. We then calculate net carrier concentrations taking into account compensating effects of oppositely charged defects. Using perturbation theory, we estimate the strength of carrier scattering of the dominant defects, to determine a relative ranking for mobility degradation of each defect.

The goal is to perform fully first principles calculations (no free parameters) to be predictive. This work is part of a larger program to study defects in a large class of semiconductors for radiation detection application using first principles computational methods, as well as predict quantitatively the related electronic transport properties (*e.g.*, $\mu\tau$). In this paper, we will focus only on the native defects in AlSb, and O and C substitutional impurities in AlSb (on the Sb site).

2.1.1 Atomic relaxation

Atomic scale models of AlSb, a binary zinc-blende alloy, and all of the defect structures were constructed and relaxed to determine the equilibrium structures. The theoretical lattice constant of AlSb was determined by performing a volume relaxation, and this value of lattice constant was used in all calculations. Models for all of the native defects (*i.e.*, those involving only the atoms in the pure compound or a lack thereof) were constructed, as well as models of O and C substitutions for Sb. Supercells of various sizes were used, ranging from 32 to 216 atoms, to enable extrapolation of defect formation energies to the infinitely dilute limit (see Sec. 2.1.2). Each supercell contained one defect. Table 1 lists all of the possible native point defects in AlSb, along with their notations. Each defect may exist in a number of charge states; generally, we have considered charge states up to $\pm 3e$. To avoid high symmetry local energy minima in the atomic relaxations, we performed multiple relaxations of each structure starting from different randomized initial configurations. Convergence to the same lowest total energy structure for each starting configuration and supercell size was confirmed. Structures that relaxed toward very different symmetry configurations (equivalent to another defect structure) were deemed unstable and discarded. Sometimes, only certain charge states of a given defect were found to be stable.

Table 1. Notation of possible native point defects in AlSb.

Symbol	Point defect type
V_{Al}, V_{Sb}	Al vacancy, Sb vacancy
Al_{Sb}, Sb_{Al}	Al antisite, Sb antisite
$Al_{i,Al}$, $Al_{i,Sb}$	Al tetragonal-site interstitials: Al-coordinated site, Sb-coordinated site
$Sb_{i,Al}$, $Sb_{i,Sb}$	Sb tetragonal-site interstitials: Al-coordinated site, Sb-coordinated site
$Al_{i,hex}$, $Sb_{i,hex}$	Al hexagonal-site interstitial, Sb hexagonal-site interstitial
$AlAl_{Al,\langle 100\rangle}$, $AlAl_{Al,\langle 110\rangle}$	Al split interstitials (intersticialcy), oriented along $\langle 100\rangle$ or $\langle 110\rangle$ directions
$SbSb_{Sb,\langle 100\rangle}$, $SbSb_{Sb,\langle 110\rangle}$	Sb split interstitials (intersticialcy), oriented along $\langle 100\rangle$ or $\langle 110\rangle$ directions
$AlSb_{Al,\langle 100\rangle}$, $AlSb_{Al,\langle 110\rangle}$	Mixed split interstitials on Al site, oriented along $\langle 100\rangle$ or $\langle 110\rangle$ directions
$AlSb_{Sb,\langle 100\rangle}$, $AlSb_{Sb,\langle 110\rangle}$	Mixed split interstitials on Sb site, oriented along $\langle 100\rangle$ or $\langle 110\rangle$ directions

2.1.2 Point defect thermodynamics

At finite temperature and in thermodynamic equilibrium, a material will contain a certain concentration of defects due to thermal activation and entropic considerations. The equilibrium defect concentration is given by[4–6]

$$C^{(q)} = C_S \theta_X^{(q)} \exp\left(-\Delta G_f^{(q)}/k_B T\right), \tag{1}$$

where $C^{(q)}$ is the concentration of a defect with charge state q, C_S is the concentration of possible defect sites, $\theta_X^{(q)}$ is the multiplicity of internal degrees of freedom of the defect on a lattice site, and $\Delta G_f^{(q)}$ is the Gibbs free energy of formation for the defect. We can split the formation free energy into three terms

$$\Delta G_f^{(q)} = \Delta E_f^{(q)} - T\Delta S_f^{(q)} + P\Delta V_f^{(q)}. \tag{2}$$

The formation enthalpy, $\Delta E_f^{(q)}$, is the dominant term, which we will refer to as the "formation energy." The formation entropy, $\Delta S_f^{(q)}$, is typically on the order of one or a few k_B, is temperature independent, and varies little between defect types or different materials. The effect of the entropy term is to nearly uniformly lower the formation free energies by on the order of 0.1 eV. The last term in Eq. (2), containing the formation volume, describes the pressure dependence of the formation free energy. The formation volume is typically a small fraction of the atomic volume, so this term can be neglected except at very high pressures.

Following the formalism of Zhang and Northrup,[7] the defect formation energy in a binary compound (specifically AlSb) is given by[8]

$$\Delta E_f^{(q)} = E_{\text{tot}}^{(q)} - \frac{1}{2}\left(n_{\text{Al}} + n_{\text{Sb}}\right)\mu_{\text{AlSb}}^{\text{bulk}} - \frac{1}{2}\left(n_{\text{Al}} - n_{\text{Sb}}\right)\left(\mu_{\text{Al}}^{\text{bulk}} - \mu_{\text{Sb}}^{\text{bulk}} + \Delta\mu\right) + q\left(E_{\text{VBM}} + \mu_e\right), \tag{3}$$

where $E_{\text{tot}}^{(q)}$ is the total energy of the defect structure (calculated by DFT), n_i denotes the number of atoms of type i in the supercell, μ_j^{bulk} is the chemical potential of component j in its reference state, E_{VBM} denotes the energy of the valence band maximum, and μ_e is the chemical potential of the electron reservoir (also referred to as the Fermi level). The parameter $\Delta\mu$ is defined to describe variations in the chemical environment of the crystal, and is an experimental variable related to the crystal stoichiometry and external environment. The range of $\Delta\mu$ is constrained by the formation energy of AlSb, ΔH_f^{AlSb}, with $\Delta\mu = -\Delta H_f^{\text{AlSb}}$ corresponding to Al-rich conditions (typical growth conditions) and $\Delta\mu = +\Delta H_f^{\text{AlSb}}$ corresponding to Sb-rich conditions (typical annealing conditions).

The main computational task for determining $\Delta E_f^{(q)}$ for each defect and charge state is to accurately calculate a set of $E_{\text{tot}}^{(q)}$ values. However, the supercell approximation (periodic boundary conditions) which we employ is susceptible to certain systematic errors from spurious interactions between defects and their periodic images, especially for charged defects—so called "finite-size effects".[9,10] For neutral defects, the leading error is due to elastic interactions. Linear elasticity theory shows that the strain energy of a point-like inclusion in a homogeneous medium falls off approximately $\propto L^{-3}$, where L is the separation between periodic images.[11,12] For periodic arrays of charge densities (or points), the interaction can be expressed as a multipole expansion.[13] The leading term is the monopole-monopole interaction, which scales as L^{-1} and can be determined analytically if the static dielectric constant of the medium and the Madelung constant of the Bravais lattice of the supercell are known. The monopole-quadrupole interaction, scaling as L^{-3}, is the next non-zero term. Higher order terms are usually small and are neglected. In our calculations of defect formation energy, we apply the monopole-monopole correction manually for each supercell size using the experimental value for the static dielectric constant ($\epsilon = 12$), and lump together the elastic and monopole-quandrupole corrections by performing a finite-size scaling with L^{-3}. In this way, we can accurately extrapolate our calculations of formation energy to the infinitely dilute limit, with very small extrapolation error. To perform the extrapolation, we used four supercell sizes: 32, 64, 128, and 216 atoms. We found that performing this careful extrapolation to infinite dilution was necessary to obtain reliable and accurate values for the formation energies.

2.1.3 Self-consistent defect and net carrier concentrations

With the formation energies for all defects under all possible charge states calculated, we can use Eq. (1) to determine the equilibrium concentration of each defect and the sum of total defects in the material, as a function of temperature for given conditions of $\Delta\mu$ and μ_e. Actually, $\Delta\mu$ is a free parameter related to the experimental conditions, but μ_e is partially determined by the concentrations of defects themselves. We can see that Eqs. (1) and (3) are not independent if we consider the charge neutrality condition. Each charged defect will contribute q free electrons to the crystal. The net free charge (accounting for the concentrations of the charged defects through Eq. (1)) is accommodated by shifting μ_e to maintain charge neutrality, via

$$n(\mu_e) = \int_{\text{CBM}}^{+\infty} D(E) f(E;\mu_e) dE \tag{4a}$$

$$p(\mu_e) = \int_{-\infty}^{\text{VBM}} D(E)\left(1 - f(E;\mu_e)\right) dE \tag{4b}$$

$$p(\mu_e) + N_D + \sum_{j,q} C_{j;\mu_e}^{(q)} q = n(\mu_e) + N_A. \tag{4c}$$

In Eqs. (4), n and p denote free electron and hole concentration, respectively; $D(E)$ is the density of states (determined with DFT on a fine energy scale using a dense *k*-point mesh); $f(E)$ is the Fermi function with μ_e as a parameter; N_D and N_A denote the concentration of intentional extrinsic donor (*n*-type) and acceptor (*p*-type) dopants, respectively; and C_j is the concentration of defect j from Eq. (1). We have explicitly indicated the μ_e dependencies in Eqs. (4).

We solve Eqns. (1), (3), and (4c) self-consistently to determine μ_e and the equilibrium defect concentrations for a given $\Delta\mu$ and T. After self-consistency is reached, the net carrier concentration can be found by subtracting Eq. (4b) from

Eq. (4a), where a positive number indicates excess holes and a negative number indicates excess electrons. Intentional extrinsic doping through N_A and N_D can be used to bias μ_e toward the VBM (*p*-type doping) or the CBM (*n*-type doping), respectively, but a self-consistent solution of the charge neutrality condition accounting for any charged defects is still required to determine the correct value of μ_e. In general, only the defects with the lowest formation energies (within a range of a few tenths of an electron-volt) will significantly affect the total defect and net carrier concentrations.

2.1.4 Defect scattering of charge carriers

To estimate the effect on carrier mobility of a given defect, we calculate the scattering rate due to the presence of the defect in the crystal (in the dilute limit). Through first order perturbation theory in the Born approximation, Fermi's Golden Rule gives the scattering rate, R, due to the potential perturbation, ΔV, induced in the perfect crystal by the presence of the defect:[14]

$$R = \frac{2\pi}{\hbar} \left| \langle \psi_f^{\mathbf{k'}} | \Delta V | \psi_i^{\mathbf{k}} \rangle \right|^2 \delta \left(\epsilon_f - \epsilon_i \right). \tag{5}$$

Here, $\hbar$ is the reduced Planck's constant, ψ_i and ψ_f are, respectively, initial and final state wavefunctions corresponding to momentum states **k** and **k'**, with ϵ_i and ϵ_f initial and final state (eigen)energies; $\delta(\cdot)$ denotes the Dirac delta function. We determine ΔV by taking the difference in real space of the self-consistent local potential in a supercell containing the defect and the potential in a same-sized supercell of the perfect crystal. In principle, we need to calculate the scattering rate for every possible (elastic) scattering event among the set of ψ. The mobility can be determined from the scattering rates through the Boltzmann transport equation, which shows an approximate proportionality between mobility and the inverse of the scattering rates.[14] From a band structure calculation, we can calculate the carrier mobilities fully from first principles, however, in practice the task is computationally very expensive due to the need to perform a 3D reciprocal space integral of the scattering rates given in Eq. (5), which requires a very dense *k*-point mesh. An efficient means to calculate the large number of matrix elements is needed.

However, to obtain the relative effect of different defects on the mobility, we do not need to perform the full quantitative calculation. Instead, we can estimate the strength of the perturbation potential acting on the wavefunctions. Since the wavefunctions ψ are orthonormal, the matrix elements in Eq. (5) only have contributions from gradients of ΔV. Thus, we define a relative perturbation potential strength for a given defect as

$$M = \int \left| \nabla_{\mathbf{r}} (\Delta V) \right| d\mathbf{r}, \tag{6}$$

where $\nabla_{\mathbf{r}}$ denotes the gradient operator and $|\cdot|$ indicate taking the absolute value.

2.1.5 Computational details

All DFT total energy calculations were carried out using the Vienna *ab initio* Simulation Package (VASP)[15–18] and the projector augmented-wave method (PAW).[19,20] The local density approximation (LDA)[21] of Ceperley and Alder[22] as parameterized by Perdew and Zunger[23] was used for the exchange-correlation functional. Brillouin zone integrations were performed with Monkhorst-Pack (MP)[24] *k*-point grids using Gaussian smearing with a width of 0.1 eV. For the 32- and 64-atom supercells, $6 \times 6 \times 6$ MP grids were used; for the 128-atom supercells, $3 \times 3 \times 3$ MP grids were used (shifted off Γ); for the 216-atom supercells, $4 \times 4 \times 4$ MP grids were used. Pseudopotentials supplied with VASP were used, with a plane-wave energy cutoff of 300 eV for native AlSb calculations; for calculations involving O or C, a cutoff of 400 eV was used. Ionic relaxations were continued until all forces were below 20 meV/Å. All calculations were performed at the theoretical equilibrium volume. For the charged defects, the total number of electrons in the calculation was adjusted to create the charged state, with a compensating homogenous background charge added to maintain overall charge neutrality in the supercell.

2.2 Experimental Methods

2.2.1 AlSb growth

We grow single crystal boules of AlSb using the Czochralski method in a sealed system. The starting material consists of pellets of 99.9999% pure Sb melted into a solid ingot in a quartz ampoule, and 99.9999% pure Al. The process of melting Sb in the quartz ampoule introduces oxygen into the ingot and visibly etches the quartz leaving bubbles on the surface of the Sb ingot; we refer to this process as the "Q process." The Al is melted in an Al_2O_3 crucible and held for 24 h to outgas

the oxide, before introduction of the Sb ingot. Heating is performed by a graphite susceptor separated from the Al_2O_3 crucible by 1 atm continuous flow of Ar gas. Optionally, 3–4% of H_2 gas may be flowed with the Ar to help reduce oxides. Nucleation is controlled by a seed crystal, which is pulled from the melt at $\sim$1 cm/h while rotating at 2 rpm. Growth is performed at 1330 K. Some samples are subjected to post-growth annealing up to 1200 K with Sb overpressure for up to 8 d. We have achieved highly reproducible, large single crystal growths up to $\sim$20 cm^3 showing excellent uniformity and few, if any, macroscopic defects. High purity boules up to 900 g can be grown with greater than 80 wt% utilization of starting material.

2.2.2 Defect and carrier concentration measurements

X-ray diffraction and Laue measurements are routinely used to determine crystallinity and orientation of the grown AlSb boules. High-resolution transmission electron microscopy (HRTEM) studies confirm excellent single crystallinity. Samples are sawed and polished for analysis and electrical characterization, minimizing air exposure to prevent surface oxidation. Dynamic secondary ion mass spectrometry (dynamic SIMS) is used on all samples to determine the concentrations of impurity atoms. SIMS surveys covering a broad range of the periodic table provide initial screening for detectable impurities before more careful measurements are performed for the major impurities. Electrical characterization is performed with room temperature Hall measurements, which reveal net carrier concentration, carrier type, resistivity, and majority carrier mobility for each sample.

3. RESULTS

3.1 Defect structures

We studied the atomic structure and stability of all native defects in AlSb, accounting for charge states from -3 to $+3$, and also O and C substitutional impurities on the Sb site. We know that the "Q process," where the starting Sb material is melted in a quartz ampoule, introduces O into our material. The hot graphite susceptor is a source of C impurity.

Most of the native defects are stable in at least one charge state. Only $Al_{i,hex}$ and $AlSb_{Al,\langle 100\rangle}$ are not stable at all. These defects spontaneously lowered their energies by transforming into a different defect. We tested the relative stability of both C and O impurities for substitution on either the Sb or Al site. Both O and C prefer to substitute on the Sb site, gaining 2–3 eV in stability compared to Al substitution. Thus, O is a single-donor dopant, while C is a single-acceptor dopant. We note that C, as a group IV element, is a potentially amphoteric dopant, but since it strongly prefers to substitute Sb, it will generally act as a *p*-type dopant. The stable charge states of all of the defects we examined are summarized in Table 2.

Table 2. Stable defects in AlSb (refer to Table 1 for notation).

Defect	Stable Charge States	Defect	Stable Charge States
V_{Al}	$0, -1, -2, -3$	$^*Al_{Al,\langle 100\rangle}$	$+2, +1, 0, -1, -2$
V_{Sb}	$+1, 0, -1, -2, -3$	$^*Al_{Al,\langle 110\rangle}$	$+2, +1, 0, -1, -2$
Al_{Sb}	$0, -1, -2, -3$	$^*Sb_{Sb,\langle 100\rangle}$	$+2, +1$
Sb_{Al}	$+2, +1, 0$	$^*Sb_{Sb,\langle 110\rangle}$	$+2, +1, 0, -1, -2$
$Al_{i,Al}$	$+2, +1, 0, -1, -2$	$^*AlSb_{Al,\langle 110\rangle}$	$+1, 0, -1, -2$
$Al_{i,Sb}$	$+2, +1, 0, -1, -2$	$AlSb_{Sb,\langle 100\rangle}$	$0, -1, -2$
$Sb_{i,Al}$	$+2, +1, 0, -1, -2$	$AlSb_{Sb,\langle 110\rangle}$	$+2, +1, 0, -1, -2$
$Sb_{i,Sb}$	$+2$	C_{Sb}	-1, substitutes Sb
$Sb_{i,hex}$	$+1, 0, -1, -2$	O_{Sb}	$+1$, substitutes Sb

*Metastable

The structures of the vacancies and antisite defects maintain their original site symmetry, except for the Sb vacancies which exhibit a Jahn-Teller distortion for all but the $+1$ charge state. Similarly, all of the stable tetrahedral and hexagonal interstitials maintain their site symmetries, except for the $Sb_{i,Al}$ which also undergo Jahn-Teller distortions. Most of the split interstitials are unstable or metastable (see Table 2). Only the mixed split interstitials on the Sb site have stable charge states. Many of the metastable split interstitials can transform into either a tetrahedral interstitial or another split interstitial with little or no energy barrier. Further details of the split interstitial structures and relative stabilities will be presented in a future paper.

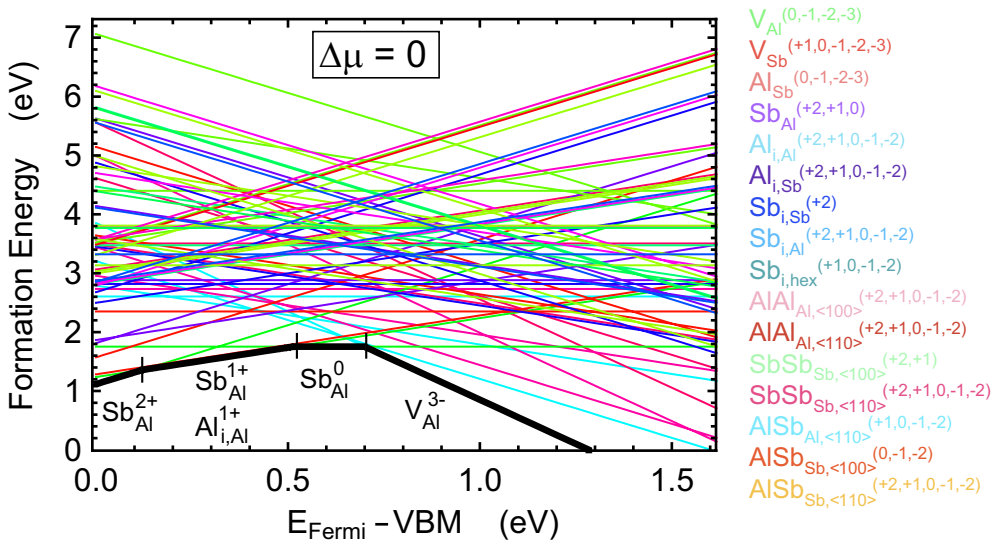

Fig. 1. (Color) Calculated formation energies of all stable or metastable native point defects in AlSb, for $\Delta\mu = 0$ (stoichiometric conditions), as a function of Fermi level throughout the band gap. The lowest E_f states are highlighted by the bold line at the bottom, with the corresponding defects in each segment labeled below. Important low-formation energy lines are extracted in detail in Fig. 2, for the limiting cases of $\Delta\mu$.

For the impurity atoms, the C substitution on Sb was well-behaved with no significant symmetry breaking, but the O substitution underwent a large structural change during relaxation. The O atom moved into the center of the triangle formed by three nearest neighbor Al atoms, forcing the fourth Al neighbor to bond more strongly to its three Sb nearest neighbors. Strong distortion of the second nearest neighbors accompanied the relaxation. The O substitution retains the expected $+1$ charge state and acts as an *n*-type dopant.

3.2 Defect formation energies

We calculated the formation energies for all of the stable and metastable native point defects in AlSb (listed in Table 2) following Eq. (3). We re-emphasize that the formation energies depend on the parameters μ_e and $\Delta\mu$, which correspond, respectively, to the doping level (net carrier concentration) in the material and the chemical environment. As described in Section 2.1.3, μ_e is not entirely a free parameter, due to the inherent dependence on the charged defect concentrations and their formation energies. However for high purity material relevant for radiation detection application, μ_e tends to remain close to mid-gap. The parameter $\Delta\mu$ is free to vary, but the practical values lie at the extreme limits, which correspond to either Al-rich conditions ($\Delta\mu = -\Delta H_f^{\mathrm{AlSb}}$) or Sb-rich conditions ($\Delta\mu = +\Delta H_f^{\mathrm{AlSb}}$). Since the AlSb phase diagram dictates that melt growth will always exhibit slight non-stoichiometry favoring excess Al, growth conditions correspond to the Al-rich limit. On the other hand, annealing conditions can be varied to control $\Delta\mu$ during post-growth processing; typically, Sb overpressure (the Sb-rich limit) is employed to minimize sublimation of the high vapor pressure Sb from the crystal surface and also to promote filling of Sb vacancies that resulted from the Al-rich growth.

The results of the formation energy calculations for the native defects are summarized in Fig. 1, for the case of $\Delta\mu = 0$. The data are plotted as a function of μ_e (or $\mathrm{E_{Fermi}}$) throughout the band gap, where 0 eV corresponds to the valence band maximum (VBM) and 1.61 eV corresponds to the conduction band minimum (CBM). In principle, μ_e can span the energy range of the band gap, depending on external doping levels, but as explained in the previous paragraph the interesting values of μ_e for our case lie near mid-gap at $\sim$0.8 eV.

We see for each type of defect a set of lines corresponding to different slopes given by the charge state, q, via Eq. (3). Wherever two lines with different q cross, for a single defect type, defines a set of ionization energies, where it becomes energetically favorable for a defect to acquire a new charge state. If ionization occurs within the band gap, the defects generally can be classified into two types depending on whether the change in charge is positive or negative at ionization:

positive-type defects tend to be donor states and describe CBM-derived states; negative-type defects tend to be acceptor states and describe VBM-derived states. The defect classification is important because of the well-known LDA band gap problem, which significantly underestimates the experimental gap.[25,26] In the case of AlSb, the LDA gap we calculate (at 0 K) is 1.12 eV, while the experimental gap at room temperature is 1.61 eV. With knowledge of the experimental band gap, we can employ the so-called "scissors operator" to shift the conduction band states upwards in energy to open the gap.[26] However, when applying the scissors operator, we need to be careful about properly shifting the ionization energies, which were calculated within the LDA gap. A judicious approach consists of rigidly shifting the donor-like ionization energies with the CBM, while keeping the acceptor-like ionization energies tracking the VBM.[27] This is the approach we have adopted.

In interpreting the results summarized in Fig. 1, which appears quite complicated at first glance, we make note of the fact that only the very lowest formation energy defects will contribute appreciably to the concentration of defects or carriers in the material (at equilibrium), since E_f appears in the exponential in Eq. (1). Thus, in the figure, a bold line is drawn connecting the lowest E_f states throughout the range of E_{Fermi}, and the segments are labeled with the particular defect that is dominant. In the case shown for $\Delta\mu = 0$, two defects exhibit nearly degenerate E_f between $\mu_e \sim$ 0.1–0.5 eV, so both defects are indicated. For high purity radiation detector material, we find the dominant defect to be V_{Al}^{3-}. The large negative q implies a strong self–hole-doping behavior, and the zero crossing of E_f within the gap indicates a tendency to pin the Fermi level. While the majority of defects shown in Fig. 1 have E_f values too large to significantly contribute to total defect densities or net carrier densities in the material, many of the higher E_f defects comprise deep level traps that can affect carrier lifetime and reduce the $\mu\tau$ figure of merit for radiation detection devices. Detailed analysis of the trapping contributions of the defects will appear in a future publication.

Since we are concerned mostly with the lowest E_f defects, we can simplify Fig. 1 in consideration of the effect of varying $\Delta\mu$, which we show in Fig. 2. The set of dominant defects varies somewhat from the Al-rich limit to the Sb-rich limit, although V_{Al}^{3-} is always an important defect. Conditions are evident where the antisite defects as well as the $Al_{i,Al}$ interstitial can also play a role.

With all of the formation energies known, we apply Eq. (1) self-consistently as described in Section 2.1.3 to obtain the total equilibrium defect concentration in the material at various temperatures. We can regard the temperature parameter as describing annealing temperatures, since as-grown material is expected to be in nonequilibrium and driven toward equilibrium by heat treatment. The equilibrium concentration represents a lower bound. Figure 3 shows the results, taking into account all of the stable and metastable native defects in AlSb, but assuming no extrinsic doping (pure material).

3.3 Mobility

We calculated perturbation potentials ΔV for the dominant native defects in AlSb, as well as for C and O impurities. We then applied Eq. (6) to calculate relative strengths of the perturbations to deduce each defect's relative contribution to mobility degradation, normalized by concentration. The results of these calculations are shown in Fig. 4. We see that the O impurity exhibits a scattering strength more than 5× stronger than the other defects, due to the significant structural rearrangement that occurs around the O defect and the consequent longer-range distortions of the lattice (see Sec. 3.1). Oxygen acts as a strong mobility killer. In general, the impurity defects show stronger scattering than the native defects.

As mentioned earlier, for ultrapure material at moderate temperatures (*e.g.*, room temperature), the upper limit of mobility is determined by electron-phonon scattering. Our calculations of this upper limit from first principles is beyond the scope of the present discussion and will be presented in a future publication. However, previous estimates place the room temperature upper bounds in the range of up to ∼1000 cm^2/V-s for both electrons and holes, with holes thought to have a slightly lower mobility.[28]

3.4 Experimental results

We are generally able to grow large single-crystal boules of AlSb with ppb impurity concentrations reproducibly. Impurities consist of only low-Z elements, with C, O, Si, and S comprising the major constituents. Typical concentrations of these elements as measured by SIMS are C $\sim 5 \times 10^{16}$ cm^{-3}, O $< 1 \times 10^{15}$ cm^{-3} (below detection limit), Si $\sim 5 \times 10^{15}$ cm^{-3}, and S $\sim 2 \times 10^{16}$ cm^{-3}. Mobility greater than 400 cm^2/V-s has been achieved. The measured characteristics of a few representative samples are summarized in Table 3. Generally, we find that the Q process leads to higher resistivity, but also higher total defect density. Adding 3–4% H_2 to the growth atmosphere reduces the total defect density by about an order of magnitude, but also leads to lower resistivity material. However, the as-grown mobility of the H_2-reduced material tends to

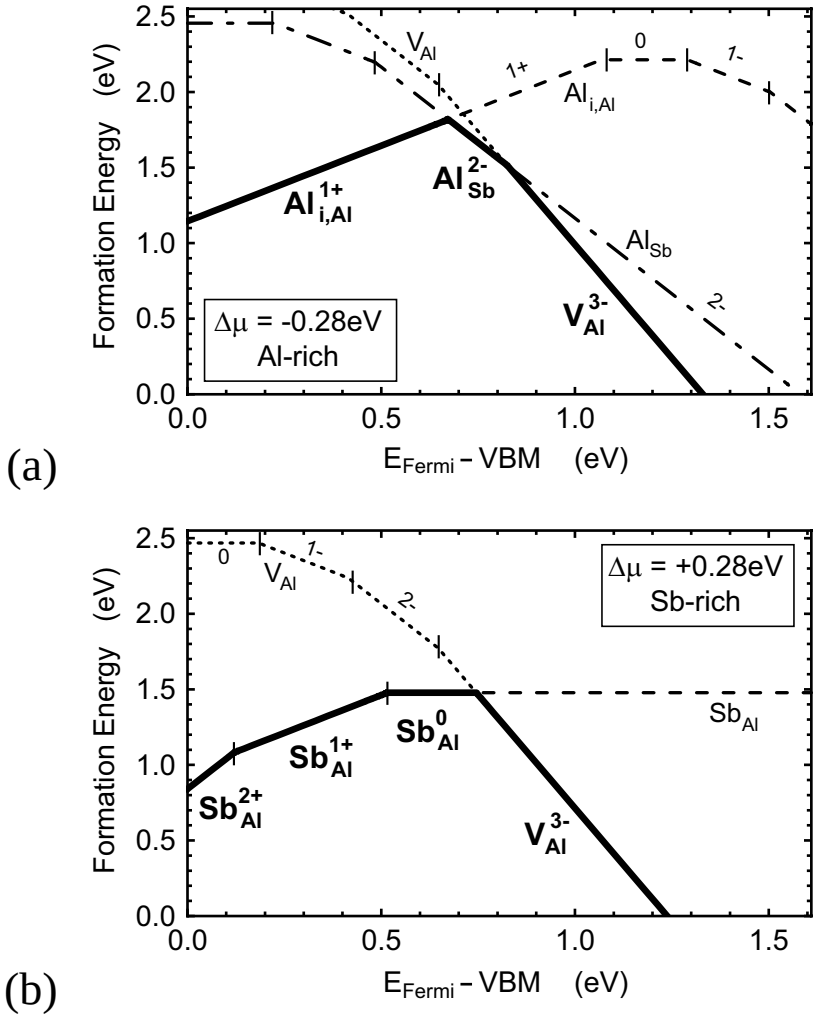

Fig. 2. Low formation energy defects extracted from Fig. 1 for (a) $\Delta\mu = -0.276$ (Al-rich limit) and (b) $\Delta\mu = +0.276$ (Sb-rich limit), as a function of Fermi level throughout the band gap. Ticks indicate ionization energies.

be quite high. The mobility of material grown from the Q process can be significantly improved by annealing, for example at 1200 K for 8 d with Sb overpressure, to values over 100 cm^2/V-s. The mobility improvement upon annealing is achieved with little change in either net carrier density or total defect density. The net carrier density tends to be much lower for Q process material compared to H_2-reduced material by over an order of magnitude.

Table 3. Measured properties of AlSb samples from Hall and dynamic SIMS.

Sample	**Type**	**Resistivity (Ω-cm)**	**Mobility (cm^2/V-s)**	**Net Carrier Density (cm^{-3})**	**Total Defect Density (cm^{-3})**
Q process as-grown	*n*-type	1.5×10^4	18	2.3×10^{13}	3.1×10^{16}
Q process annealed	*n*-type	3.5×10^3	130	1.4×10^{13}	$\approx 4 \times 10^{16}$
H_2-reduced #1	*p*-type	9.7×10^1	350	2.4×10^{14}	4.0×10^{15}
H_2-reduced #2	*p*-type	1.8×10^1	450	8.9×10^{14}	—

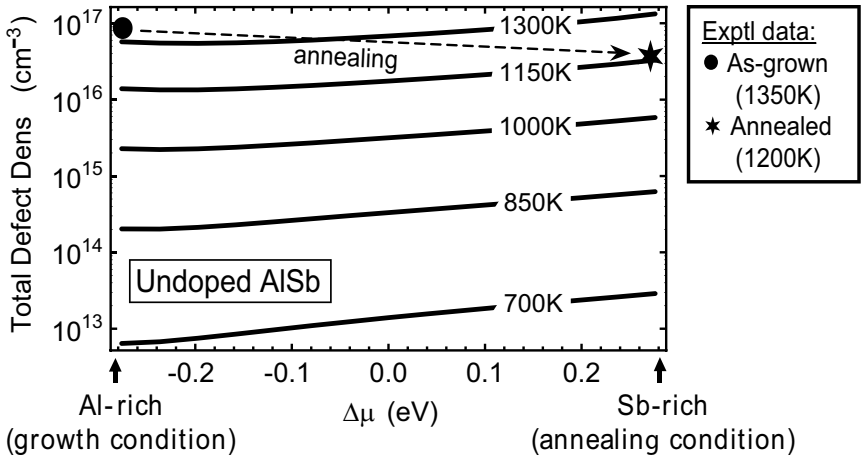

Fig. 3. Total equilibrium defect concentration calculated self-consistently, accounting for all native defects in AlSb and assuming no extrinsic doping, as a function of chemical environment with temperature as a parameter.

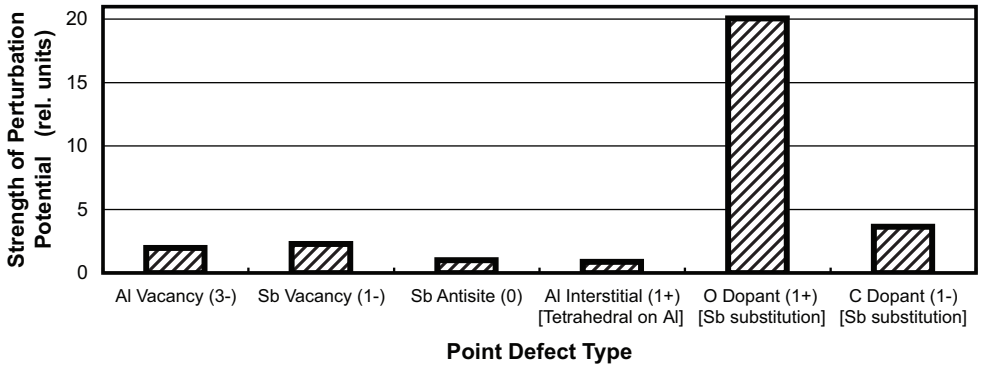

Fig. 4. Estimated relative mobility degradation for the dominant point defects in AlSb.

4. DISCUSSION

The results we have obtained build a clear understanding of the role of defects – both native and impurity – in the variability of material performance of AlSb for radiation detection application, as well as provide direct guidance toward optimization. The equilibrium native defect concentrations calculated provide a lower bound for total defect densities at different annealing temperatures. While kinetics need to be considered to plan an optimal annealing time, the results here give a maximum temperature allowed to achieve a desired defect level (in the long time limit). Insight into the thermodynamic effects of the annealing environment is revealed as well. In general, these types of calculations are helpful for screening purposes, since they provide a gating criterion (minimum practical achievable defect density) for an experimental effort. The results presented here demonstrate the very good predictive power of our theory, illustrated by the agreement with experimental measurements of defect concentrations shown in Fig. 3. The bold circle in the upper left of Fig. 3 marks a measured value of total defect concentration of high quality as-grown material (grown at 1330 K), in close agreement with the calculated value at 1300 K under Al-rich conditions. After annealing at 1200 K for 8 d with Sb overpressure, this sample showed a reduction in total defect concentration, indicated by the bold star at the upper right of Fig. 3. Again, the agreement is quite good, matching closely with the calculated value at 1150 K for Sb-rich conditions. The result also indicates that the annealing step was successful in driving the material nearly to equilibrium.

But not all defects are alike. Neutral defects contribute to the total defect concentration, but do not contribute to net carrier concentration. Also, positively and negatively charged defects contribute oppositely to carrier concentration, compensating each other. Furthermore, if we examine the energy levels of different defects, we expect shallow defects to be easily ionized

and contribute fully to carrier density, however deep levels may not be ionized. (We are further interested in deep levels for their trapping characteristics, as mentioned earlier, but this aspect is beyond the current discussion.) In the case of high purity AlSb, we are particularly interested in the interplay between V_{Al}^{-3} and O_{Sb}^{+1}. The V_{Al}^{-3} is a strong *p*-type self-dopant, while the O_{Sb}^{+1} is an extrinsic (impurity) *n*-type dopant. We know from the results in Fig. 4 that O is a strong mobility killer. Thus, it is possible to drastically reduce net carrier concentration by the incorporation of O and increase resistivity, but this greatly reduces mobility. We notice this effect in the experimental data highlighted in Table 3. The H_2-reduced growths eliminate much of the O impurity, leading to the highest mobilities even without annealing; however, the carrier densities are one to two orders of magnitude higher compared to the Q process growths and the material exhibits correspondingly low resistivity. Also, the H_2-reduced material is *p*-type, since the O does not compensate the self-doping from the V_{Al}^{-3} (as well as any *p*-type doping from C impurities). Conversely, Q process growths produce *n*-type material due to high excess O content, along with correspondingly low mobilities. The compensating effect is evident in the much higher total defect densities coupled with much lower net carrier densities. Furthermore, annealing improves mobility considerably. The precise details of this process require further study, but a likely contribution comes from the preference of O to form stable oxides with Al and Sb rather than remain as a substitutional defect. Also, the usual annealing process takes the as-grown material from the Al-rich limit to the Sb-rich limit, increasing somewhat the equilibrium V_{Al}^{-3} concentration. We have calculated the O phase stability diagram in AlSb to determine limits for O substitutional incorporation, and the results (1×10^{14} – 1×10^{16} cm^{-3} range) are consistent both with the doping levels required for the explanations given here and also the measured limits of O impurity levels. Additionally, experiments have been performed to intentionally dope AlSb highly with O to give high resistivity material. The approach succeeds, but at the expense of obtaining negligible mobility, as we expect. In fact, one needs to be careful about using resistivity to characterize material, since it is only loosely related to mobility (the more pertinent property), as demonstrated in this particular example of a compensating dopant that is also a mobility killer.

Finally, concerning the compensation doping by O, our calculations show that much higher levels of O are required to make the material *n*-type under Sb-rich conditions compared to Al-rich conditions. The reason is the lower concentration of V_{Al} under Al-rich conditions, which reduces the self–*p*-doping and Fermi level-pinning. Thus, it might be possible to lower the net carrier density and increase resistivity, with a lower concentration of O, yielding higher mobility. We are investigating this idea further.

5. CONCLUSIONS

We have used first principles calculations of defects in AlSb, coupled with experimental growth efforts, to gain insight into the microscopic mechanisms of material degradation. The results of our study are leading to improved material through optimized growth and post-growth processes. We have demonstrated the quantitative predictive ability of our calculations of defect and carrier densities. Through scattering rate calculations, we have shown that O is a particularly strong mobility killer and its incorporation into the crystal should be minimized. This result leads to better understanding of seemingly conflicting experimental data, which sometimes show variations in mobility and carrier concentration that do not track each other or the resistivity. There is a fundamental tradeoff between the carrier compensation effect of O impurities and the strong mobility degradation associated with O.

In addition to continuing to explore the effects of various defects and phonons on optimizing AlSb material, we are expanding our efforts to other materials of interest as well, with the goal of working toward the ability to perform computational materials discovery experiments. We are developing fully first principles approaches to quantitatively predict the properties of materials and alloys (*e.g.*, mobility, lifetime, and defect levels) that are relevant to a specific application, such as gamma radiation detection, and use that capability to find optimal materials as well as to guide experimental efforts at growth and process optimization.

ACKNOWLEDGMENTS

This work was performed under the auspices of the U.S. Dept. of Energy at the University of California/Lawrence Livermore National Laboratory under contract no. W-7405-Eng-48. The authors acknowledge support from the National Nuclear Security Administration (NNSA) Office of Nonproliferation Research and Development (NA-22). Some original concepts and ideas for this work were internally funded by the Laboratory Directed Research and Development (LDRD) Program at LLNL.

REFERENCES

1. A. Owens, "Semiconductor materials and radiation detection," *J. Synchrotron Rad.* **13**, pp. 143–150, 2006.
2. G. A. Armantrout, S. P. Swierkowski, J. W. Sherohman, and J. H. Lee, "What can be expected from high-Z semiconductor detectors," *IEEE Trans. Nucl. Sci.* **N5-24**, pp. 121–125, 1977.
3. K. Hecht *Z. Phys.* **77**, p. 235, 1932.
4. P. M. Fahey, P. B. Griffin, and J. D. Plummer, "Point defects and dopant diffusion in silicon," *Rev. Mod. Phys.* **61**, pp. 289–384, 1989.
5. R. A. Swalin, *Thermodynamics of Solids*, Wiley, New York, 1962 (second edition).
6. A. R. Allnatt and A. B. Lidiard, *Atomic Transport in Solids*, Cambridge University Press, Cambridge, 2003.
7. S. B. Zhang and J. E. Northrup, "Chemical potential dependence of defect formation energies in GaAs: Application to Ga self-diffusion," *Phys. Rev. Lett.* **67**, pp. 2339–2342, 1991.
8. G.-X. Qian, R. M. Martin, and D. J. Chadi, "First-principles study of the atomic reconstructions and energies of Ga- and As-stabilized GaAs(100) surfaces," *Phys. Rev. B* **38**, pp. 7649–7663, 1988.
9. Y.-J. Zhao, C. Persson, S. Lany, and A. Zunger, "Why can $CuInSe_2$ be readily equilibrium-doped n-type but the wider-gap $CuGaSe_2$ cannot?," *Appl. Phys. Lett.* **85**, pp. 5860–5862, 2004.
10. P. Erhart, K. Albe, and A. Klein, "First-principles study of intrinsic point defects in ZnO: Role of band structure, volume relaxation, and finite-size effects," *Phys. Rev. B* **73**, p. 205203, 2006.
11. D. Grecu and P. H. Dederichs, "The asymptotic behaviour of the displacement field of point defects in 'isotropic' crystals," *Phys. Lett. A* **36**, pp. 135–136, 1971.
12. P. H. Dederichs and J. Pollman *Z. Physik* **255**, p. 315, 1972.
13. G. Makov and M. C. Payne, "Periodic boundary conditions in ab initio calculations," *Phys. Rev. B* **51**, pp. 4014–4022, 1995.
14. M. H. Evans, X.-G. Zhang, J. D. Joannopoulos, and S. T. Pantelides, "First-principles mobility calculations and atomic-scale interface roughness in nanoscale structures," *Phys. Rev. Lett.* **95**, p. 106802, 2005.
15. G. Kresse and J. Hafner, "Ab initio molecular dynamics for liquid metals," *Phys. Rev. B* **47**, pp. 558–561, 1993.
16. G. Kresse and J. Hafner, "Ab initio molecular-dynamics simulation of the liquid-metal–amorphous-semiconductor transition in germanium," *Phys. Rev. B* **49**, pp. 14251–14269, 1994.
17. G. Kresse and J. Furthmüller, "Efficiency of ab-initio total energy calculations for metals and semiconductors using a plane-wave basis set," *Comput. Mater. Sci.* **6**, pp. 15–50, 1996.
18. G. Kresse and J. Furthmüller, "Efficient iterative schemes for ab initio total-energy calculations using a plane-wave basis set," *Phys. Rev. B* **54**, pp. 11169–11186, 1996.
19. P. E. Blöchl, "Projector augmented-wave method," *Phys. Rev. B* **50**, pp. 17953–17979, 1994.
20. G. Kresse and J. Joubert, "From ultrasoft pseudopotentials to the projector augmented-wave method," *Phys. Rev. B* **59**, pp. 1758–1775, 1999.
21. L. Hedin and B. I. Lundqvist, "Explicit local exchange-correlation potentials," *J. Phys. C* **4**, pp. 2064–2083, 1971.
22. D. Ceperley and B. Alder, "Ground state of the electron gas by a stochastic method," *Phys. Rev. Lett.* **45**, pp. 566–569, 1980.
23. J. Perdew and A. Zunger, "Self-interaction correction to density-functional approximations for many-electron systems," *Phys. Rev. B* **23**, pp. 5048–5079, 1981.
24. H. J. Monkhorst and J. D. Pack, "Special points for Brillouin-zone integrations," *Phys. Rev. B* **13**, pp. 5188–5192, 1976.
25. R. W. Godby, M. Schlüter, and L. J. Sham, "Accurate exchange-correlation potential for silicon and its discontinuity on addition of an electron," *Phys. Rev. Lett.* **56**, pp. 2415–2418, 1986.
26. R. W. Godby, M. Schlüter, and L. J. Sham, "Self-energy operators and exchange-correlation potentials in semiconductors," *Phys. Rev. B* **37**, pp. 10159–10175, 1988.
27. J. T. Schick, C. G. Morgan, and P. Papoulias, "First-principles study of As interstitials in GaAs: Convergence, relaxation, and formation energy," *Phys. Rev. B* **66**, p. 195302, 2002.
28. C. Kittel, *Introduction to Solid State Physics*, p. 221. Wiley, New York, 1996 (seventh edition).